Exploring Electrochemical C(sp³)−H Oxidation over Fe Complexes: Ligand Effect on the Rate−Bond Dissociation Energy Relationship and Reaction Mechanism

Yu-Wei Chuang,[§] Kuan-Yu Lu,[§] Chien-Wen Lin,[§] Yung-Ching Yang, Yun-Jou Tseng, Hao-Ting Chang, Ting-Yee Chuang, Tzuhsiung Yang, I-Chung Lu, and Yu-Heng Wang*

Cite This: ACS Catal. 2025, 15, 9106−9116

Read Online

ACCESS | ⬛ Metrics & More | 📖 Article Recommendations | 🆘 Supporting Information

ABSTRACT: Fe complexes **1** and **2**, bearing tetraamido macrocyclic ligands (TAMLs) with different π-conjugation arrangements, were prepared as molecular catalysts to investigate the influence of the ligand on the efficacy of the electrochemical C(sp³)−H-oxidation reaction. Pourbaix diagrams revealed that catalyst **2**, with extended π-conjugation in its TAML, reached a higher oxidation state under a lower potential and generated different reaction intermediates. The catalytic performances were assessed using the linear free energy relationship; that is, the dependence of the logarithm of the second-order catalytic rate constant ($\log(k_{cat})$) on the C(sp³)−H bond dissociation energy ($BDE_{(Csp^3−H)}$) of organic substrates. The slope of the relationship between $\log(k_{cat})$ and $BDE_{(Csp^3−H)}$ was notably shallower for catalyst **2** compared to catalyst **1**, reflecting a reduced sensitivity to substrate $BDE_{(Csp^3−H)}$. This behavior is attributed to the greater ligand π-conjugation of **2** that the high-valent Fe-oxo active species is therefore more stable and

less electrophilic, resulting in a smaller difference in the k_{cat} than **1** for different substrates. This study explicitly reveals that modifications in ligand architecture can directly modulate catalytic activity and alter reaction pathways in the electrochemical C(sp³)−H-oxidation by iron-based molecular catalysts.

KEYWORDS: C(sp³)−H-oxidation reaction (CHOR), electrocatalysis, tetraamido macrocyclic ligands (TAMLs), earth-abundant molecular catalyst, linear free energy relationship (LFER)
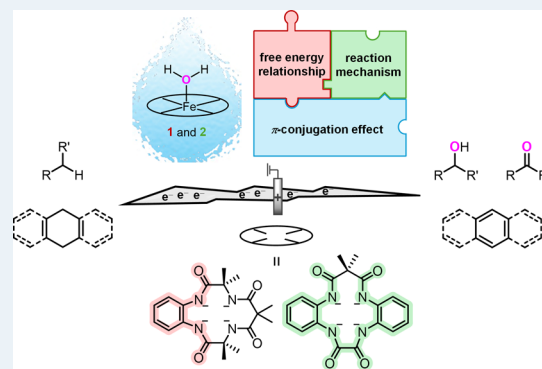
1. INTRODUCTION

The C(sp³)−H-oxidation reaction (CHOR) is vital in energy conversion, the oxidative transformation of natural gas into valuable commodities, and biofuel production from biomass.[1,2] However, the inherent stabilities and low reactivities of C(sp³)−H bonds present significant challenges in the CHOR, necessitating the use of harsh conditions, such as excess sacrificial oxidants (e.g., H_2O_2, AcO_2H, PhIO, and mCPBA), high-cost precious-metal catalysts, and high reaction temperatures. Such challenges limit the development of advanced technologies and synthetic methodologies.[3−6] The utility of electrocatalysis in the CHOR has recently received renewed attention.[7−9] Leveraging the principles of electrochemical techniques to activate and functionalize inert C(sp³)−H bonds under mild conditions, electrocatalysis offers numerous advantages over traditional methods.[10,11] Unlike heterogeneous catalysts, molecular catalysts are characterized by their well-defined molecular structures, which enable in-depth investigations into the reaction mechanisms using spectroscopic and analytical techniques.[12,13] In addition, the catalytic activities of molecular catalysts can be fine-tuned with

ligand modification in the primary and secondary coordination spheres.[14−18] These unique attributes of molecular catalysts are ideal for integration with the study of electrocatalytic CHOR.

Fe complexes can form Fe(IV)− and Fe(V)−oxo intermediates, which are oxidatively active toward inert C(sp³)−H bonds by using sacrificial oxidants in previous studies.[19−24] The ligands of molecular Fe complexes are crucial in generating high-valent Fe−oxo intermediates and durable electrocatalysts. For example, strongly electron-donating ligands can stabilize the electron-deficient Fe center, thereby preventing catalyst degradation.[25,26] Additionally, the ligand may engage in a redox process through metal−ligand cooperation, facilitating the formation of high-valent Fe intermediates by lowering the overall oxidation potential.[27−29]
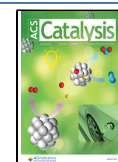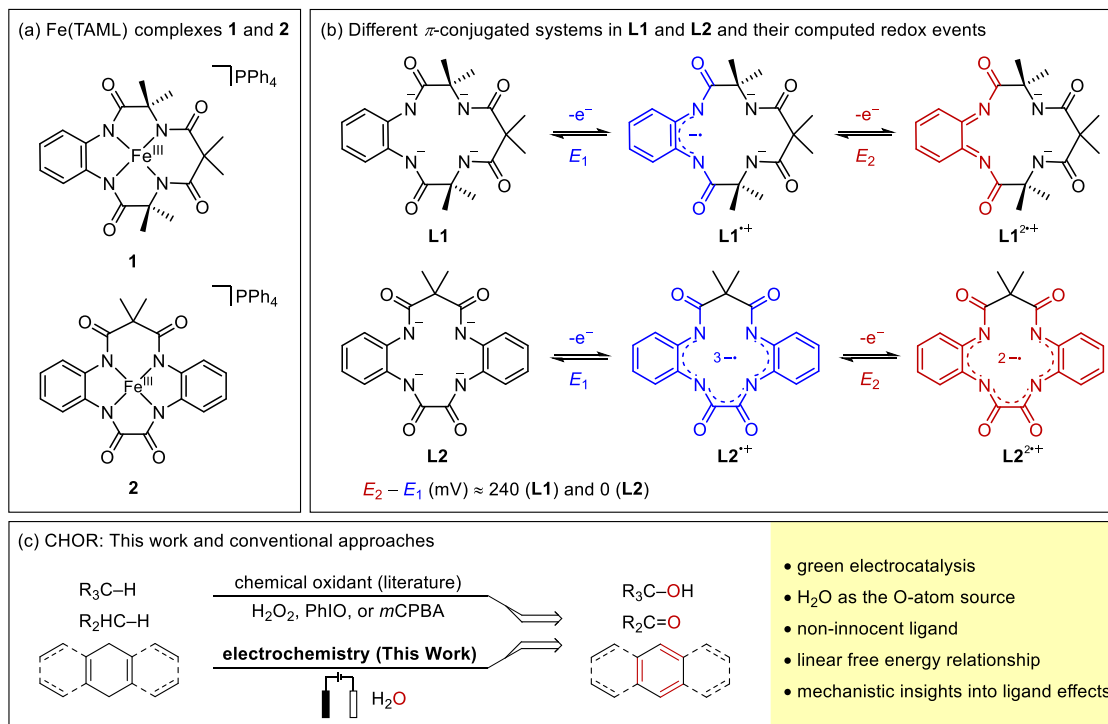
Scheme 1. Catalysts 1 and 2 and Redox Properties of L1 and L2[a]

[a](a) Fe(TAML) complexes used in this study (PPh$_4$: tetraphenylphosphonium). (b) Schematic of the non-innocent features of **L1** and **L2** and the computed ΔE values of the two successive redox events for **L1** and **L2** (see Section S12 for details). (c) Highlights and significance of this work compared to conventional approaches.

Such ligands are known as (redox) noninnocent ligands and include tetraamido macrocyclic ligands (TAMLs). The non-innocent redox capacities of TAMLs have been applied in redox chemistry, as exemplified by recent studies of nitrene formation,[27] H$_2$O-oxidation,[28] and nucleophilic substitution.[29] These characteristics suggest that Fe(TAML) complexes are promising C(sp^3)−H-oxidation (electro)catalysts (CHOCs).[30,31]

Based on the noninnocent capacities of TAMLs, utilizing a TAML with more extensive π-conjugation is expected to facilitate the formation of high-valent Fe−oxo intermediates at lower oxidation potentials by better stabilizing the resulting oxidative species.[15−18] Here, two Fe(TAML) complexes (**1** and **2**; Scheme 1a) with different π-conjugated systems in their TAMLs (**L1** and **L2**) were prepared as CHOCs. In **L1**, the π-conjugation extends across half of the macrocyclic ring, whereas the conjugation within **L2** is more extensive, covering >75% of the ligand framework. The variation in ligand structure results in distinct potential difference values for their two successive redox events (ca. 240 mV (**L1**) vs. ca. 0 mV (**L2**) in Scheme 1b; see Section S12 for details). Crucially, the electrochemical behaviors of **1** and **2** are expected to be affected by the redox properties of TAMLs, leading to changes in the reactivity and reaction mechanism of the CHOR.

In this study, the electrochemical oxidation of **1** and **2** in the presence of H$_2$O yields high-valent Fe-oxo adducts by harnessing H$_2$O as the oxygen source, which is employed to examine CHOR under mild conditions (Scheme 1c). The influence of the TAML on the catalytic efficacy of **1** and **2** is assessed using the linear free energy relationship (LFER) between the logarithm of the reaction rate constant ($\log(k_{cat})$) and C(sp^3)−H bond dissociation energy (BDE$_{(Csp^3−H)}$) of the

substrates being investigated.[32,33] The observation highlights the electrophilicity of active Fe-oxo species, which is affected by the ligand motif and has a profound impact on the $\log(k_{cat})$−BDE$_{(Csp^3−H)}$ correlation. The catalytic cycles are proposed on the basis of spectroscopic evidence and computational approaches, and the differing reaction intermediates of **1** and **2** may cause notable disparities in their reactivity with specific substrates.

2. RESULTS

2.1. Synthesis, Stability, and Electrochemical Properties of 1 and 2. To investigate the effect of the ligand type on the electrochemical CHOR, sample pairs with different degrees of π-conjugation, i.e., H$_4$**L1**,[34] H$_4$**L2**,[35] **1**,[36,37] and **2**[35] (Scheme 1), were prepared by following established procedures. The identities of **1** and **2** were initially confirmed by their distinctive Fe isotope patterns identified using electrospray ionization mass spectrometry (ESI-MS). The molecular structure of **1** was characterized via X-ray diffraction, which affirmed the presence of aqua axial ligands attached to the central Fe atoms (Section S14). Although the crystal structure of **2** could not be obtained, its purity was verified using elemental analysis (Section S2b). The electrochemical behaviors of **1** and **2** were evaluated using cyclic voltammetry (CV) with a three-electrode system comprising a glassy carbon working electrode, Pt wire counter electrode, and Ag/AgCl reference electrode containing 3 M KCl (unless otherwise stated, all potentials are reported with respect to the Ag/AgCl potential). In acetonitrile (MeCN), **1** and **2** exhibited two quasi-reversible redox couples (**1**: 0.61 and 1.19 V; **2**: 0.65 and 1.07 V), corresponding to the respective 1 e$^−$ redox processes of Fe$^{III/IV}$ and Fe$^{IV/V}$ (Figure 1a,b, black traces).[38,39] In
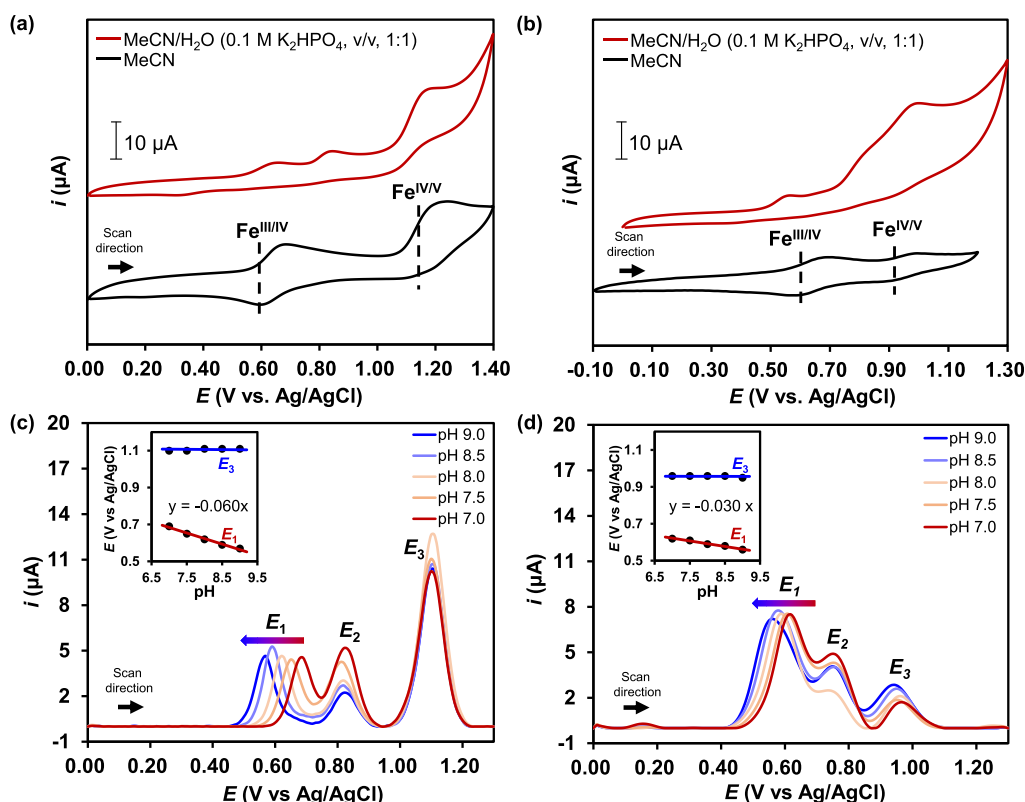
Figure 1. Electrochemical properties of **1** and **2**. Cyclic voltammograms of 0.5 mM (a) **1** and (b) **2** in MeCN and 0.1 M K_2HPO_4 in a 1:1 (v/v) ratio of MeCN/H_2O. In the presence of a phosphate buffer, the redox event at ~0.80 V indicates Fe-HPO_4^{2-} complexation.[38,39] All cyclic voltammograms were recorded under 1 atm N_2 at a scan rate of 100 mV s^{-1}. Supporting electrolyte: 0.1 M $LiClO_4$. The cyclic voltammograms were plotted using the International Union of Pure and Applied Chemistry (IUPAC) conventions. Differential pulse voltammograms (DPV) of 0.5 mM (c) **1** and (d) **2** in a 1:1 (v/v) ratio of MeCN/H_2O with 0.1 M phosphate buffer (pH 7−9). Inset: Pourbaix diagrams of **1** and **2**. See Section S4a for the DPV parameters.

contrast, Fe-HPO_4^{2-} complexation resulted in an additional redox peak at ~0.80 V in a buffer containing 1:1 (v/v) MeCN/H_2O with 0.1 M K_2HPO_4 (Figure 1a,b, red traces).[38,39]

The quasi-reversible potentials of **1** and **2** in the buffered solution indicate that these oxidation potentials may not be solely attributable to electron-transfer processes. Thus, differential pulse voltammetry (DPV) was employed to obtain Pourbaix diagrams of **1** and **2** between pH 7.0 and 9.0 to clarify these redox events (Figure 1c,d). As shown in Figure 1c, the 1 e$^-$/1H$^+$ stoichiometry of the first oxidation potential of **1** is implied based on the slope of 0.060 V pH^{-1} (E_1), corresponding to **L1**Fe^{III}−OH_2 (**1**)/**L1**Fe^{IV}−OH (**1a**). The second oxidation potentials (E_2) of **1** and **2** are due to the phosphate-ligated Fe(TAML) complexes in the presence of the phosphate buffer (Figure 1a,b, ca. 0.80 V in the red traces).[38,39] The subsequent oxidation potential at 1.1 V (E_3) is independent of the pH in the range of 7.0−9.0, and is primarily assigned to the 1 e$^-$ process of **1a**/**L1**Fe^V−OH (**1b**). However, **2** shows distinct behavior compared to **1**. The involvement of a 2 e$^-$/1H$^+$ process in the first redox event of **2** is indicated by the slope of 0.030 V pH^{-1} (Figure 1d, E_1), which is tentatively ascribed to **L2**Fe^{III}−OH_2 (**2**)/**L2**$^{\bullet+}$Fe^{IV}−OH (**2a**).[40] The redox event at 1.0 V (E_3) is likely due to the single-electron oxidation of **2a** to **L2**$^{\bullet+}$Fe^V−OH (**2b**, Figure 1d), because E_3 is invariant over the measured pH range. The difference in the total stoichiometric electron−proton transfer between **1** (2 e$^-$/1H$^+$) and **2** (3 e$^-$/1H$^+$) suggests that different types of Fe intermediates are formed under these

electrochemical conditions. Accordingly, the Fe center of **2** should result in a higher oxidation state than that of **1**, but the E_3 of **2** (ca. 0.95 V) is approximately 100 mV lower than that of **1** (ca. 1.1 V). However, this result is not surprising considering that **L2** acts as a better redox reservoir compared to **L1**, as shown in Scheme 1b.

2.2. Kinetic Studies: Reaction Rate Law and the CHOR vs the Water Oxidation Reaction. A reaction mixture composed of **1** and diphenylmethane (DPM) in 1:1 (v/v) MeCN/H_2O and K_2HPO_4 (0.1 M) was used to investigate the effects of the catalyst and substrate concentrations using CV. DPM was chosen as a substrate due to its moderate BDE$_{(Csp^3−H)}$[41] and expected reactivity. Under these catalytic conditions, catalytic currents (i_c) for **1** are observed at the potential of the Fe^{IV}/Fe^V redox couple (Figure 2a,c, 1.25 V). Plots of i_c at the potential of the Fe^{IV}/Fe^V redox couple as functions of the catalyst concentration or square root of the substrate concentration (Figure 2b,d, respectively) are linear, showing that the CHOR follows second-order kinetics (eqs 1−3; see Section S5 for the kinetic studies of **2**).[42,43]

$$i_c = n_c FAC_{cat}\sqrt{D_{cat}k_{obs}} \tag{1}$$

$$k_{obs} = k_{cat}C_{sub} \tag{2}$$

$$\text{Rate}_{(CHOR)} = k_{cat}[\text{cat}][\text{sub}] \tag{3}$$

Here, n_c, F, A, C_{cat}, C_{sub}, D_{cat}, k_{obs}, and k_{cat} refer to the number of electrons involved in the catalytic wave, Faraday's constant (96,485 C mol^{-1}), electrode surface area (2.25 × 10^2
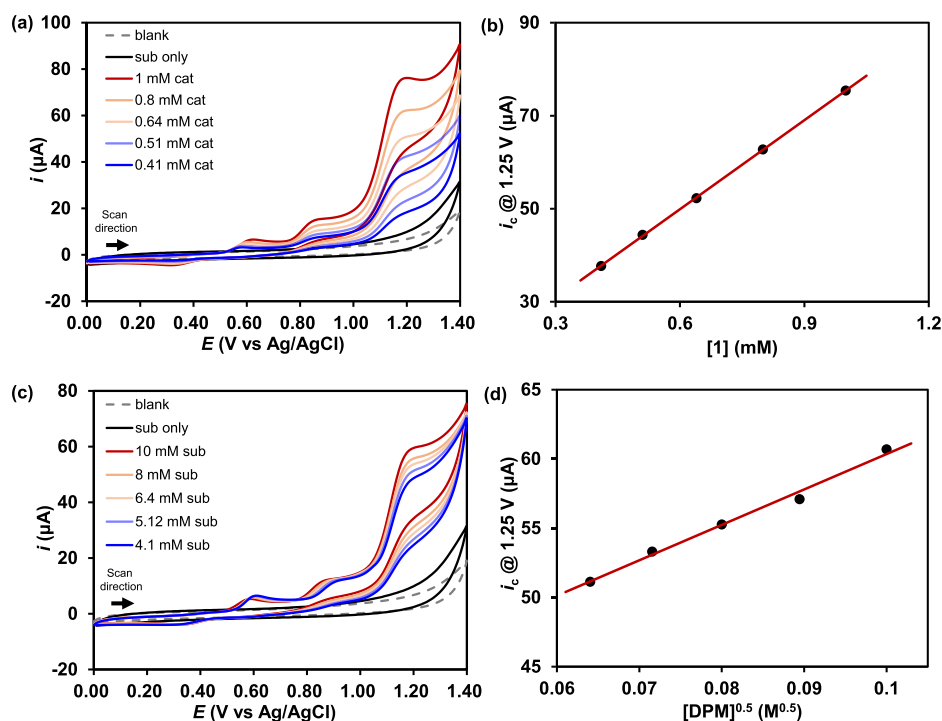
Figure 2. Kinetic studies of electrochemical CHOR. (a) Cyclic voltammograms of **1** at various concentrations (0.41−1 mM) in the presence of 10 mM DPM. (b) Anodic catalytic current derived from the CV results as a function of the concentration of **1**. (c) Cyclic voltammograms of 1 mM **1** in the presence of various concentrations of DPM (4.1−10 mM). (d) Anodic catalytic current derived from the CV results as a function of the DPM concentration. General conditions: 0.1 M K_2HPO_4 in 5 mL of 1:1 (v/v) $MeCN/H_2O$ at a scan rate of 100 mV s^{-1}. The cyclic voltammograms are plotted using the IUPAC conventions.

Table 1. $\log(k_{cat})$ and $BDE_{(C_{sp}^3-H)}$ Values of 1 and 2[a]

substrate	BDE (kcal mol^{-1})	n_c	k_{cat} (M^{-1} s^{-1})		$\log(k_{cat})$ (M^{-1} s^{-1})	
			1	2	1	2
H_2O		4	8.4×10^{-2}	4.1×10^{-1}	−1.08	−0.38
xanthene	75.2[b]	4	2.1×10^2	2.6×10^1	2.16	1.41
DHA	76.3[b]	7.2 (**1**)5.5 (**2**)	1.3×10^2	5.8×10^0	2.61	0.82
2-indanone	79.1[b]	4	3.0×10^0		0.48	
fluorene	79.5[c]	4	1.0×10^1		1.0	
anthrone	80.2[d]	4	3.7×10^{-1}	4.4×10^0	−0.43	0.64
DPM	82.0[c]	4	3.6×10^{-1}		−0.44	
tetralin	82.9[b]	4	1.7×10^0	2.3×10^0	0.22	0.35
indane	85.3[b]	4	2.1×10^{-1}	1.1×10^0	−0.69	0.050

[a]General conditions: [**1**] = [**2**]: 0.25 mM, [substrate]: 2.5 mM, solvent: 1:1 (v/v) $MeCN/H_2O$ with 0.1 M K_2HPO_4 at 25 °C. DHA: dihydroanthracene. DPM: diphenylmethane. The determination of k_{cat} is described in Section S10. [b]See Table 1 of ref 35. [c]See Table 2 of ref 35. [d]See ref 64. The standard deviations of the k_{cat} were calculated to be approximately 5% for **1** and **2** from triplicate determinations.

π cm^2), catalyst (mol cm^{-3}) and substrate concentrations (M), diffusion coefficient of the catalyst (cm^2 s^{-1}), pseudo-first-order rate constant (s^{-1}), and second-order catalytic rate constant (M s^{-1}), respectively. D_{cat} was determined via the Randles–Sevcik equation (Section S4c), and k_{obs} is equivalent to the turnover frequency. In this study, the n_c values for selected substrates were determined based on the product selectivity, and the oxidized products were characterized using ^1H and ^{13}C nuclear magnetic resonance (NMR) and electron ionization mass spectrometry (EI-MS). See Table S5 and Section S13 for experimental details.

Kinetic isotope effect (KIE) studies using CV with D/H-labeled substrates were conducted to elucidate the turnover-limiting step (TLS). D/H-labeled xanthenes were utilized in the KIE study because xanthene-d_2 can be synthesized

according to a reported protocol (Section S2c). The slope of the normalized current (i_c/i_p) as a function of the inverse square root of the scan rate ($\nu^{-1/2}$) was used to estimate the average KIE[44] using eqs 4 and 5 (Section S6).

$$\frac{i_c}{i_p} = \frac{2.24 n_c}{n_p^{3/2}} \sqrt{\frac{RT k_{obs}}{F \nu}} = \frac{0.359 n_c}{n_p^{3/2}} \sqrt{\frac{k_{obs}}{\nu}} \tag{4}$$

$$KIE = k_{cat(H)}/k_{cat(D)} = slope_{(H)}^2/slope_{(D)}^2 \tag{5}$$

here, n_p, R, T, ν, $k_{cat(H)}$, and $k_{cat(D)}$ are the number of electrons involved in the noncatalytic wave, ideal gas constant (8.3145 J K^{-1} mol^{-1}), reaction temperature (K), scan rate (V s^{-1}), and catalytic rate constants with H- and D-labeled xanthene, respectively. The large KIE values of **1** (9.6) and **2** (8.4) imply
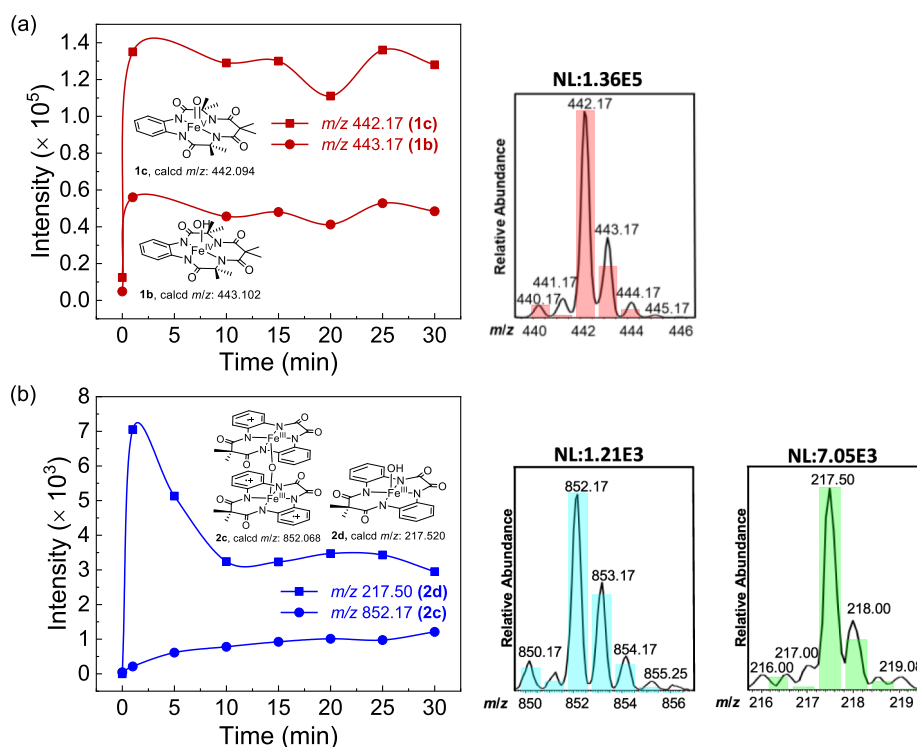
https://doi.org/10.1021/acscatal.5c01183
ACS Catal. 2025, 15, 9106−9116

Figure 3. Time-dependent CSI-MS peak intensities for (a) **1** and (b) **2** at −5 °C. General conditions: [**1**] = [**2**]: 0.2 mM, [NBu$_4$IO$_4$]: 0.4 mM, [K$_2$HPO$_4$]: 0.01 mM, solvent: 1:1 (v/v) MeCN/H$_2$O. The theoretical isotopic distributions of **1b**, **1c**, **2c**, and **2d** are provided in Section S11. Normalization level (NL): relative ion intensity of the base peak.
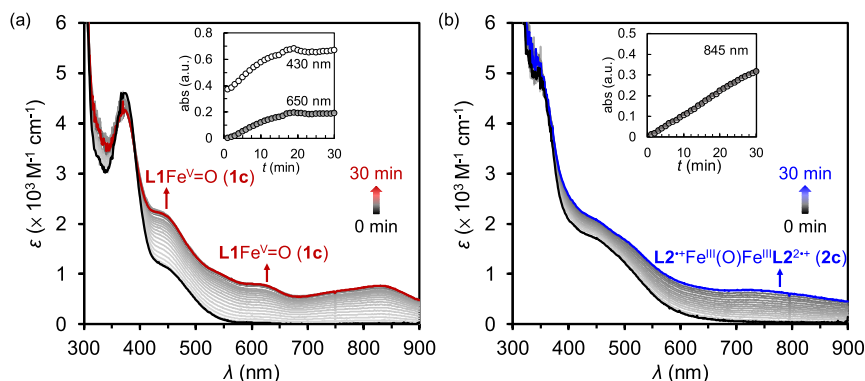

Figure 4. Time-dependent UV−vis spectra of CHOR catalyzed by (a) **1** with DPM and (b) **2** with tetralin, under 1 atm N$_2$ at 0 °C. General conditions: [**1**] = [**2**]: 0.3 mM, [NBu$_4$IO$_4$]: 3 mM, [DPM] = [tetralin]: 3 mM, [K$_2$HPO$_4$]: 5 mM, solvent: 19:1 (v/v) MeCN/H$_2$O.
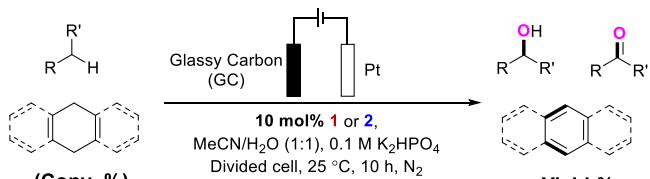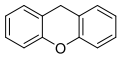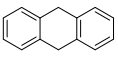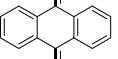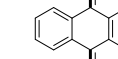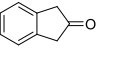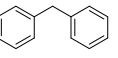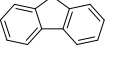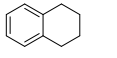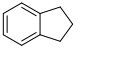
that C(sp^3)−H bond cleavage is the TLS, which occurs via hydrogen atom transfer (HAT).[45,46]

The WOR may be competitive with the CHOR under the reaction conditions employed in this study, because the formed Fe−oxo intermediates are potentially active toward water oxidation.[32,47] In the absence of organic substrates with reaction conditions analogous to the CHOR, the electrochemical results show that the WOR exhibits first-order kinetics with respect to the catalyst and H$_2$O concentrations, leading to an overall second-order rate law (Section S8). The detection of O$_2$ evolution indicates that the n_c of the WOR is ~4 for both **1** and **2** (Section S9b). The k_{cat} of the WOR was derived from the current of the catalytic plateau (eqs 1 and 2; Section S8).[48] The reaction kinetics of the CHOR and WOR were compared based on their k_{cat} values. It is noteworthy that the k_{cat} values of the WORs catalyzed by **1** and **2** are 2−3 orders of magnitude lower than those of the CHORs with

xanthene as the substrate (CHOR: 2.1(6) × 10^2 M s^{-1} (**1**) and 2.6(2) × 10^1 M s^{-1} (**2**); WOR: 8.4(2) × 10^{-2} M s^{-1} (**1**) and 4.1(3) × 10^{-1} M s^{-1} 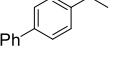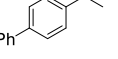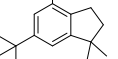(**2**); see Table 1 and Sections S8−S10 for details). This comparison shows that the WOR is kinetically sluggish compared to the CHOR under analogous electrochemical conditions.

2.3. Mechanistic Investigation of the CHOR. To further examine the Fe species of **1** and **2** under oxidative conditions, a reaction mixture containing 0.2 mM **1** and 0.4 mM NBu$_4$IO$_4$ in 1:1 (v/v) MeCN/H$_2$O with 0.01 mM K$_2$HPO$_4$ was initially probed in situ using negative-ion-mode cold-spray ionization mass spectrometry (CSI-MS) at −5 °C (Section S11). The electrochemical conditions used for CV and DPV (0.1 M K$_2$HPO$_4$) are unsuitable for CSI-MS because the MS capillary can be blocked by concentrated K$_2$HPO$_4$. Therefore, the K$_2$HPO$_4$ solution was diluted to 0.01 mM for CSI-MS measurements. The anionic forms of the Fe species of **1** are

Table 2. Substrate Scope of C(sp³)−H Bond Oxidation Catalyzed by 1 and 2[a]

Reaction scheme: R–CH(R')–H (with dihydroacene backbone), Glassy Carbon (GC) | Pt electrodes, 10 mol% **1** or **2**, MeCN/H₂O (1:1), 0.1 M K₂HPO₄, Divided cell, 25 °C, 10 h, N₂ → products R–CH(OH)–R' and R–C(O)–R' (Yield %); substrate marked (Conv. %).

Entry	Conversion (1 / 2)	Yield (1 / 2)
a (xanthene → xanthone)	(>99%)[a] / (91%)[a]	87% (n_c: 4)[a] / 85% (n_c: 4)[a]
b-i (→ anthracene)	(>99%)[a] / (88%)[a]	13%[a] / 34%[a]
b-ii (→ anthraquinone)		86% (n_c: 7.2)[a] / 47% (n_c: 5.5)[a]
b-ii (→ anthrone)	(>99%)[a] / (>99%)[a]	92% (n_c: 4)[a] / 94% (n_c: 4)[a]
c (indanone → indan-1,2-dione)	(96%)[a]	89% (n_c: 4)[a]
d (diphenylmethane → benzophenone)	(85%)[a]	74% (n_c: 4)[a]
e (fluorene → fluorenone)	(>99 %)[a]	91% (n_c: 4)[a]
f (tetralin → α-tetralone)	97%[b] / (>99%)[b]	94% (n_c: 4)[b] / 96% (n_c: 4)[b]
g (indane → indanone)	(70%)[a] / (74%)[a]	62% (n_c: 4)[a] / 73% (n_c: 4)[a]
h-i (4-ethylbiphenyl → ketone)	(70%)[a,c]	53%[a,c]
h-ii (→ alcohol)		10% (n_c: 3.7)[a,c]
i (substituted indane → indanone)	(91%)[a,c]	85% (n_c: 4)[a,c]

[a] Assay yield and conversion were determined by ¹H NMR spectroscopy with 1,3,5-trimethoxybenzene as an internal standard and gas chromatography (GC) with bromobenzene as an internal standard. [b] NMR yield. [c] GC yield. [d] Reaction time: 20 h. See Section S9 for details.

observed at m/z 443.17 ($z = -1$) and 442.17 ($z = -1$), assigned as **1b** and **1c**, respectively. The time-course concentration profiles further reveal that the intensities of the peaks related to these two species are reasonably constant over the 30 min reaction time (Figure 3a and Section S11). This indicates that **1b** and **1c** are steady-state intermediates under these conditions. **L1Fe^V=O** (**1c**) is proposed to be the primary active species for the CHOR.[39,49−52]

Complex **2** shows a different type of oxidized Fe species than that observed in **1**. The mass spectrograms suggest that **L2Fe^{IV}−OH** and **L2Fe^V=O** are not the dominant species under the same conditions because the peak intensities of **L2Fe^{IV}−OH** ($m/z = 434.17$) and **L2Fe^V=O** ($m/z = 435.25$) are below the reliable detection limit of CSI-MS (Section S11). A further signal appears at m/z 852.17 ($z = -1$) is assigned to **L2$^{•+}$Fe^{III}−O−Fe^{III}L2$^{2•+}$** (**2c**, Figure 3b), as suggested by density functional theory (DFT) analysis (Tables S16,S17). Conversely, the amount of analogous μ-oxo-bridged di-iron species of **1** is negligible relative to **1b** or **1c**, as indicated by the mass spectrograms (Figure S27). The prevalent formation of **2c** seems to occur via the reaction between electrophilic **2b** and deprotonated **2** (**L2Fe^{III}−OH**, **2d**), along with the release of 1 equiv of H₂O.[47] The presence of **2d** is confirmed by the signal observed at m/z 217.50 ($z = -2$, Figure 3b).

The Fe intermediates involved in the CHORs catalyzed by **1** and **2** were subsequently analyzed in situ using ultraviolet−visible (UV−vis) spectrometry with a CoolSpek cryostat (Unisoku, Hirakata, Japan). Figure 4 shows the time-resolved UV−vis spectra of the reaction mixtures of **1** with DPM and **2** with tetralin in the presence of NBu₄IO₄ (NBu₄ = tetrabutylammonium), as an exogenous oxidant, at 0 °C. Complex **2** has little activity toward DPM under these reaction conditions (possibly because of steric hindrance), so tetralin was chosen as the substrate for the UV−vis study. The formation of **L1Fe^V=O** (**1c**) from **1** is indicated by two distinct absorption peaks at 430 and 650 nm, as well as the broad peak at 700−900 nm (Figure 4a).[53−55] By contrast, the lack of characteristic Fe^V=O peaks in the visible region of the spectrum for **2** suggests that the resulting intermediate is a μ-oxo-bridged di-iron species (**2c**, Figure 4b).[53−55]

2.4. LFER of 1 and 2. The catalytic performances of **1** and **2** toward various C(sp³)−H substrates were analyzed using the LFER (also known as the Bell−Evans−Polanyi relation).[56−58] This method offers insights into the interplay between kinetic (k_{cat}) and thermodynamic (i.e., $BDE_{(Csp^3-H)}$) parameters to evaluate the performances of **1** and **2** as CHOCs.[32] LFER analysis enables the direct comparison of the efficacies of catalysts with similar TLSs. A good (electro)catalyst should exhibit higher reaction kinetics under the conditions of minimum reaction thermodynamics.[59,60] The k_{cat} of each C(sp³)−H substrate catalyzed by **1** or **2** was calculated using the slope of the plot of i_c/i_p as a function of $\nu^{-1/2}$ (eq 4 and Section S10).[61] The $BDE_{(Csp^3-H)}$ of each substrate was retrieved from the literature.[33,62] For **1** and **2**, the n_c, k_{cat},

and $BDE_{(Csp^3-H)}$ values of each substrate are listed in Table 1, and the conversion and yield of each substrate are summarized in Table 2.

The $\log(k_{cat})$ of the CHOR is directly proportional to the $BDE_{(Csp^3-H)}$ (Figure 5), and the slope describes the depend-
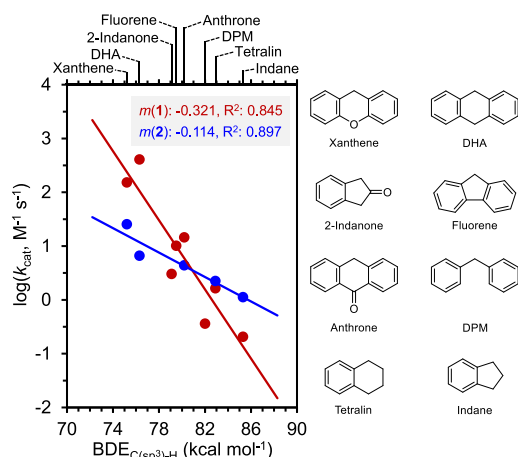

Figure 5. LFER plot of $\log(k_{cat})$ vs $BDE_{(Csp^3-H)}$ of **1** (red trace) and **2** (blue trace) in the CHOR, along with the structures of the substrates.

ence of k_{cat} on the $BDE_{(Csp^3-H)}$. The $\log(k_{cat})-BDE_{(Csp^3-H)}$ relationship of **1** displays a significantly steeper slope than that of **2** (Figure 5; $m(\mathbf{1})$: -0.321, $m(\mathbf{2})$: -0.114), and the crossover of these two linear relationships occurs at a $BDE_{(Csp^3-H)}$ of approximately 80 kcal mol^{-1}. These LFER analyses indicate that **1** is a more potent CHOC toward substrates with lower $BDE_{(Csp^3-H)}$ values (i.e., <80 kcal mol^{-1}). The shallower slope of **2** suggests that this complex is more active toward substrates with $BDE_{(Csp^3-H)}$ values of >80 kcal mol^{-1} because its reactivity is less sensitive to the $BDE_{(Csp^3-H)}$.

The chemical CHOR with the Fe^V=O form of **1** in MeCN was previously reported.[63] Although the direct comparison of k_{cat} is inaccessible due to the different reaction temperature than this study (25 °C vs −40 °C), a shallower dependence of $\log(k_{cat})/BDE_{(Csp^3-H)}$ indicates that **1** is competent to catalyze the substates with $BDE_{(Csp^3-H)}$ of 80−85 kcal/mol under electrochemical conditions (m: -0.321 vs -0.471).[34] Compared to **2**, biuret-tailed TAML-ligated Fe complexes (Fe(Me,Me-bTAML)[52] and Fe(Ph,Me-bTAML)[64]) toward chemical CHOR exhibited similar $\log(k_{cat})/BDE_{(Csp^3-H)}$ dependence (m: -0.114 vs -0.101[52] and -0.100[64]). For the substrates with $BDE_{(Csp^3-H)}$ in the range of 85−90 kcal/mol, the catalytic efficacy of **2** is comparable with Fe(Ph,Me-bTAML) but 2−3 times faster than that of Fe(Me,Me-bTAML). However, both Fe(Me,Me-bTAML) and Fe(Ph,Me-bTAML) are capable of catalyzing the substrates with $BDE_{(Csp^3-H)}$ up to ~100 kcal/mol.[34] These results disclose that the catalytic performance of Fe-oxo active species as CHOCs is also associated with the reaction media and oxidation methods in addition to ligand identity.

A few substrates could not be electrocatalyzed by either **1** or **2**, such as fluorene and 2-indanone. The rigid fluorene molecule evidently makes it difficult to access the Fe center of **2** due to steric hindrance. Additionally, the conformation of 2-indanone may lead to inevitable electrostatic repulsion between its carbonyl group and the Fe−oxo moiety of **2**, resulting in its low activity. The noncatalytic oxidation of substrates on the bare electrode prevents the LFER analysis of

substrates with $BDE_{(Csp^3-H)}$ values of <75 kcal mol^{-1}. Further investigation of the same series of Fe(TAML) complexes and C(sp^3)−H substrates under broader electrochemical conditions is in progress.

2.5. Computational Insights into the LFER. DFT calculations were subsequently performed to investigate the difference in the observed LFERs of **1** and **2**, as illustrated in Figure 5. We focused on the HAT reactions of **1** and **2** with various substrates. The studied substrates contain aryl rings that can engage in $\pi\cdots\pi$ stacking interactions with the aryl rings of **1** and **2**, and thus, we investigated the vertical and horizontal approach pathways of HAT (Figure 6 and Section S12). The
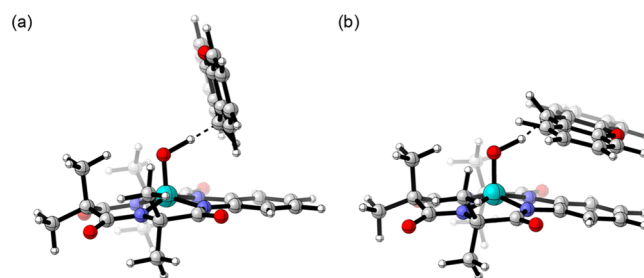

Figure 6. Transition states of (a) vertical and (b) horizontal approaches of CHOR catalyzed by **1**. The Fe, O, N, C, and H atoms are shown in cyan, red, blue, black, and white, respectively.

findings from the computations uncover that the steric hindrance of **2c** prevents substrate access to the Fe metal center. Thus, **2c** detected via CSI-MS (Figure 3b) and UV−vis spectroscopy (Figure 4b) is most likely a precatalyst. Only the mononuclear Fe intermediates of **1** and **2** are involved in the transition state (TS).

To further explore the relationship between substrate thermodynamics and reactivity, we plotted the logarithm of the calculated catalytic rate constant ($\log(k_{calcat})$), as calculated using the pathway with the lowest $\Delta G^\ddagger$, against the $BDE_{(Csp^3-H)}$ of each substrate (Figure S28). The computational results reveal a negative correlation between the $BDE_{(Csp3-H)}$ and $\log(k_{calcat})$, indicating that substrates with weaker C−H bonds generally undergo faster HAT reactions. Our calculated result shows a direct relationship between the reaction barrier of HAT and the C(sp^3)−H bond strength of the substrate. Furthermore, the slope of the LFER curve for **1** is steeper than that observed using **2**, consistent with the experimental observations (Figure S28 vs Figure 5).

The differing slopes for the CHOR catalyzed by **1** and **2** (Figure 5) may be best rationalized by the ligand effect. The enhanced π-conjugated system of **2** effectively stabilizes its Fe−oxo core and lowers its electrophilicity (Figure 1c, d, 0.95 V (**2**) vs 1.1 V (**1**)), meaning that the electrophilic activation of C(sp^3)−H bonds is less turnover-limiting at the TS compared to that of **1**. This leads to the k_{cat} of **2** being insensitive to the C(sp^3)−H bond strength, resulting in a shallower LFER slope compared to that of **1**.

2.6. Proposed Catalytic Cycles of 1 and 2. The catalytic cycles of **1** and **2** are shown in Figure 7a,b, respectively, indicating the crucial steps in converting the C(sp^3)−H substrates into the resulting oxidation products. For catalyst **1**, intermediate **1a** is generated from **1** via proton-coupled electron transfer, whereas intermediate **1b** and active species **1c** are formed through stepwise electron- and proton-transfer. The Pourbaix diagram suggests a **1** → **1a** → **1b** reaction
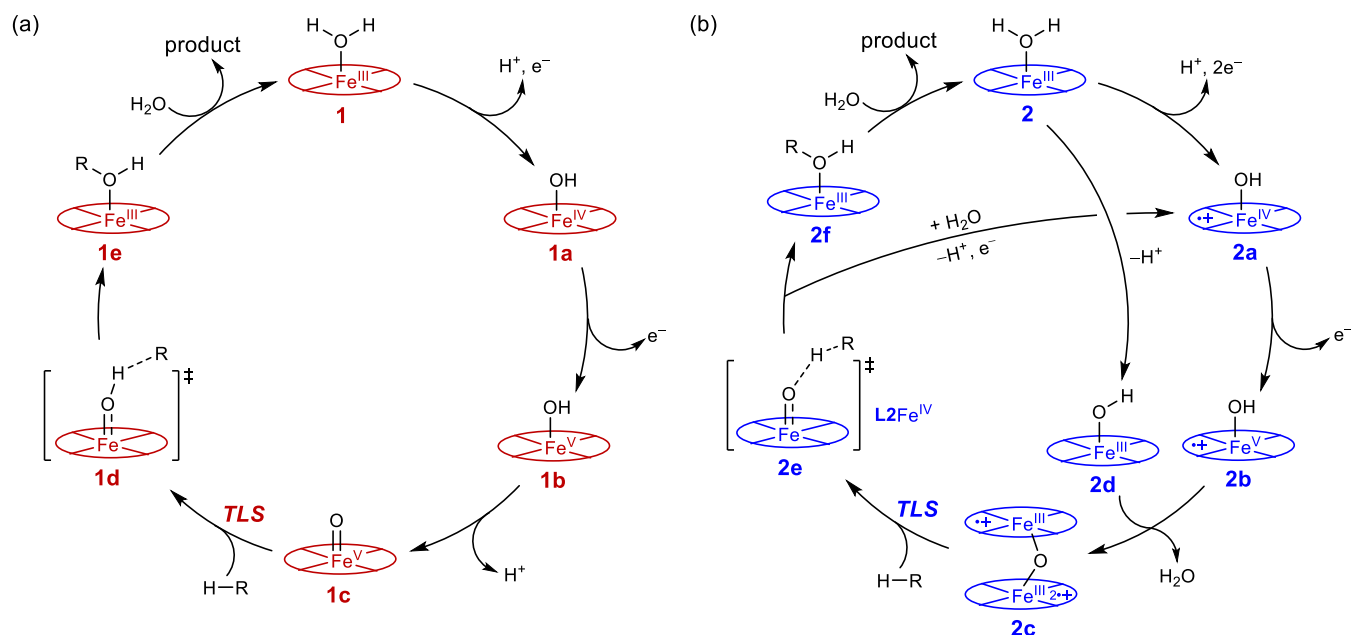
Figure 7. Proposed catalytic cycles of CHORs catalyzed by (a) **1** and (b) **2**.

pathway (Figure 1c). The high-valent Fe–oxo species **1c** activates the C(sp^3)–H substrate via HAT, which is the TLS (**1c** → **1d**). The combination of the substrate radical (R•) with **1d** leads to the bonding of the Fe^{III} intermediate and organic product (**1d** → **1e**). The subsequent nucleophilic attack with H$_2$O releases the final product and closes the catalytic cycle (**1e** → **1**).

The Pourbaix diagram of **2** suggests that **2b** and **2c** are sequentially produced from **2** under electrochemical conditions (**2** → **2a** → **2b**, Figure 1d), and the reaction between **2b** and **2d** affords the μ-oxo-bridged di-iron intermediate **2c**. The second-order rate law implies that C(sp^3)–H bond activation is the TLS, and the DFT calculations confirm that the mononuclear Fe–oxo species is involved in the TS (**2e**). Subsequent reaction with R• produces two monomeric Fe species (**2e** → **2f** and **2e** → **2a**), and H$_2$O-substitution of the bound organic product as the axial ligand completes the catalytic cycle (**2f** → **2**). These proposed catalytic cycles highlight the effects of ligand π-conjugation on the activities of TAML-based CHOCs.

3. CONCLUSIONS

The redox noninnocent characteristics of TAMLs allow for the manipulation of redox catalysis from the perspective of kinetics and thermodynamics. This study synthesized two Fe complexes, **1** and **2**, featuring TAMLs with varying extents of π-conjugation to explore the influence of ligand structure on the reactivity of electrochemical CHOR.[16,27,65] The redox behaviors of **1** and **2** were investigated using CV and DPV, and Pourbaix analysis showed that **2** undergoes a distinct 3 e$^-$/1H$^+$ redox process, attaining higher oxidation states at lower potentials due to its extended ligand π-conjugation. Kinetic studies suggested that the turnover-limiting in the reaction is HAT from the substrate by the Fe–oxo species. The catalytic effectiveness of **1** and **2** was quantitatively assessed using LFER of log(k_{cat})–BDE$_{(Csp^3–H)}$, revealing that **2** is less sensitive to the BDE$_{(Csp^3–H)}$ of substrates. This consequence could be rationalized by the differing electrophilic characteristics of their

Fe–oxo intermediates, wherein the reduced Fe-oxo electrophilicity of **2** arises from the prolonged π-conjugated **L2**.

Based on electrochemical profiles and intermediates identified through CSI-MS and UV–vis spectroscopy, specific mechanistic pathways were proposed for each catalyst. The observed different types of reaction intermediates exhibited the influence of ligand motifs on the reaction mechanisms. The computational findings add to our understanding that the mononuclear Fe-oxo is involved in the TS for both **1** and **2**. Collectively, these insights emphasize how ligand π-conjugation directly modulates catalytic properties and suggests concrete directions for optimizing catalyst performance. Future research in this field could focus on developing molecular electrocatalysts by modifying the primary and secondary coordination spheres to further refine the reactivity and selectivity in organic transformation and energy-related small molecules.

4. EXPERIMENTAL SECTION

4.1. Electrochemistry. Electrochemical studies were performed using a three-electrode apparatus and PalmSens4 potentiostat (PalmSens, Houten, Netherlands) connected to a computer running PSTrace software. All voltammetry measurements were performed under an N$_2$ atmosphere using a standard three-electrode apparatus with a glassy carbon disk and Pt wire and Ag/AgCl (3 M KCl) as the working, counter, and reference electrodes, respectively. The working electrode was polished with 0.05 μm Al$_2$O$_3$ on a wetted Buehler felt pad between each CV and DPV measurement. The laboratory temperature was maintained at 25 ± 2 °C.

4.2. Computational Methods. All DFT calculations were performed using ORCA (version 5.0.4, University of Bonn, Bonn, Germany) to examine the transfer energies of H$_2$O in various solvents. Geometry optimization was performed using the Tao–Perdew–Staroverov–Scuseria functional with the D4 dispersion correction and 6–31G* basis set. Single-point calculations were performed using the wB97X functional combined with the reparametrized D4 dispersion correction and def2-TZVPP basis set. The solvation model density

method was used to account for the solvent effects of each solvent.

ASSOCIATED CONTENT

Data Availability Statement

Requests for further information and resources should be directed to the corresponding author, Yu-Heng Wang (wangyh2@mx.nthu.edu.tw), and will be satisfied upon reasonable request. All unique materials generated in this study are available without restriction from the corresponding author. All other data supporting the findings of this study are available within the article and its Supporting Information and from the corresponding author upon reasonable request.

Supporting Information

The Supporting Information is available free of charge at https://pubs.acs.org/doi/10.1021/acscatal.5c01183.

> General instrumentation methods and experimental details, including characterization data such as electrochemical analysis of the rate constant, controlled-potential electrolysis of $C(sp^3)-H$ substrates, half-wave potentials of Fe complexes **1** and **2**, and kinetic studies of CHOR; ^1H, ^{13}C NMR spectra, and ESI-MS/HRMS of the synthesized compounds and the oxidized products (PDF)
>
> Coordinates XYZ file (ZIP)
>
> X-ray data for Fe complex **1** (CIF)

Accession Codes

Accession Codes The crystallographic data of the structures reported in this article have been deposited at the Cambridge Crystallographic Data Center (CCDC) under accession no. CCDC: 2225357 (**1**). These data can be obtained free of charge from the CCDC via http://www.ccdc.cam.ac.uk/data_request/cif.

AUTHOR INFORMATION

Corresponding Author

Yu-Heng Wang − *Department of Chemistry, National Tsing Hua University, Hsinchu 30013, Taiwan;* orcid.org/0000-0002-5655-7604; Email: wangyh2@mx.nthu.edu.tw

Authors

Yu-Wei Chuang − *Department of Chemistry, National Tsing Hua University, Hsinchu 30013, Taiwan*

Kuan-Yu Lu − *Department of Chemistry, National Tsing Hua University, Hsinchu 30013, Taiwan*

Chien-Wen Lin − *Department of Chemistry, National Tsing Hua University, Hsinchu 30013, Taiwan*

Yung-Ching Yang − *Department of Chemistry, National Chung Hsing University, Taichung 40227, Taiwan*

Yun-Jou Tseng − *Department of Chemistry, National Chung Hsing University, Taichung 40227, Taiwan*

Hao-Ting Chang − *Department of Chemistry, National Tsing Hua University, Hsinchu 30013, Taiwan*

Ting-Yee Chuang − *Department of Chemistry, National Tsing Hua University, Hsinchu 30013, Taiwan*

Tzuhsiung Yang − *Department of Chemistry, National Tsing Hua University, Hsinchu 30013, Taiwan;* orcid.org/0000-0002-6751-9806

I-Chung Lu − *Department of Chemistry, National Chung Hsing University, Taichung 40227, Taiwan;* orcid.org/0000-0002-3125-6397

Complete contact information is available at:

https://pubs.acs.org/10.1021/acscatal.5c01183

Author Contributions

§Y.-W.C. and K.-Y.L. authors contributed equally. The manuscript was written through the contributions of all authors. All authors approved the final version of the manuscript. Conceptualization, C.W.L. and Y.H.W.; methodology and investigation, Y.W.C., K.Y.L., and C.W.L.; formal analysis, Y.C.Y. (CSI-MS), Y.J.T. (CSI-MS), T.Y.C. (computations) and H.T.C. (computations); writing—original draft, Y.W.C. and K.Y.L; writing—review & editing, project administration, and funding acquisition, T.Y., I.C.L., and Y.H.W.

Notes

The authors declare no competing financial interest.

REFERENCES

(1) Sterckx, H.; Morel, B.; Maes, B. U. W. Catalytic Aerobic Oxidation of $C(sp^3)-H$ Bonds. *Angew. Chem., Int. Ed.* **2019**, *58*, 7946−7970.

(2) Gavriilidis, A.; Constantinou, A.; Hellgardt, K.; Hii, K. K.; Hutchings, G. J.; Brett, G. L.; Kuhn, S.; Marsden, S. P. Aerobic oxidations in flow: opportunities for the fine chemicals and pharmaceuticals industries. *React. Chem. Eng.* **2016**, *1*, 595−612.

(3) Junrong, H.; Min, Y.; Chuan, D.; Yajun, Z.; Huilong, F.; Lizhi, Z.; Feng, Y.; Zigang, L. Novel Strategies in C-H Oxidations for Natural Product Diversification—A Remote Functionalization Application Summary. *Front. Chem.* **2021**, *9*, 737530.

(4) Tang, X.; Jia, X.; Huang, Z. Challenges and opportunities for alkane functionalisation using molecular catalysts. *Chem. Sci.* **2018**, *9*, 288−299.

(5) Munz, D.; Strassner, T. Alkane C−H Functionalization and Oxidation with Molecular Oxygen. *Inorg. Chem.* **2015**, *54*, 5043−5052.

(6) Roduner, E.; Kaim, W.; Sarkar, B.; Urlacher, V. B.; Pleiss, J.; Gläser, R.; Einicke, W.-D.; Sprenger, G. A.; Beifuß, U.; Klemm, E.; et al. Selective Catalytic Oxidation of C−H Bonds with Molecular Oxygen. *ChemCatChem* **2013**, *5*, 82−112.

(7) Novaes, L. F. T.; Liu, J.; Shen, Y.; Lu, L.; Meinhardt, J. M.; Lin, S. Electrocatalysis as an enabling technology for organic synthesis. *Chem. Soc. Rev.* **2021**, *50*, 7941−8002.

(8) Liu, Y.; You, T.; Wang, H. X.; Tang, Z.; Zhou, C. Y.; Che, C. M. Iron- and cobalt-catalyzed $C(sp^3)-H$ bond functionalization reactions and their application in organic synthesis. *Chem. Soc. Rev.* **2020**, *49*, 5310−5358.

(9) Kawamata, Y.; Yan, M.; Liu, Z.; Bao, D.-H.; Chen, J.; Starr, J. T.; Baran, P. S. S. Scalable, Electrochemical Oxidation of Unactivated C–H Bonds. *J. Am. Chem. Soc.* **2017**, *139*, 7448–7451.

(10) Rogge, T.; Kaplaneris, N.; Chatani, N.; Kim, J.; Chang, S.; Punji, B.; Schafer, L. L.; Musaev, D. G.; Wencel-Delord, J.; Roberts, C. A.; et al. C–H activation. *Nat. Rev. Methods Primers* **2021**, *1*, 43.

(11) Thorarinsdottir, A. E.; Nocera, D. G. Energy catalysis needs ligands with high oxidative stability. *Chem Catal.* **2021**, *1*, 32–43.

(12) Zhang, L.-H.; Mathew, S.; Hessels, J.; Reek, J. N. H.; Yu, F. Homogeneous Catalysts Based on First-Row Transition-Metals for Electrochemical Water Oxidation. *ChemSusChem* **2021**, *14*, 234–250.

(13) Kokel, A.; Schäfer, C. Chapter 3.11 - Application of Green Chemistry in Homogeneous Catalysis. In *Green Chemistry*; Török, B., Dransfield, T., Eds.; Elsevier, 2018; pp 375–414.

(14) Ma, H.-C.; Hsiao, S.-C.; Wang, Y.-H. Tuning primary and secondary coordination spheres of ruthenium complexes for the homogeneous water oxidation reaction: a perspective from catalytic activity and overpotential. *Catal. Sci. Technol.* **2023**, *13*, 1598–1622.

(15) Elsby, M. R.; Baker, R. T. Strategies and mechanisms of metal–ligand cooperativity in first-row transition metal complex catalysts. *Chem. Soc. Rev.* **2020**, *49*, 8933–8987.

(16) van Leest, N. P.; de Zwart, F. J.; Zhou, M.; de Bruin, B. Controlling Radical-Type Single-Electron Elementary Steps in Catalysis with Redox-Active Ligands and Substrates. *JACS Au* **2021**, *1*, 1101–1115.

(17) Khusnutdinova, J. R.; Milstein, D. Metal–Ligand Cooperation. *Angew. Chem., Int. Ed.* **2015**, *54*, 12236–12273.

(18) Lyaskovskyy, V.; de Bruin, B. Redox Non-Innocent Ligands: Versatile New Tools to Control Catalytic Reactions. *ACS Catal.* **2012**, *2*, 270–279.

(19) Sacramento, J. J. D.; Goldberg, D. P. Factors Affecting Hydrogen Atom Transfer Reactivity of Metal–Oxo Porphyrinoid Complexes. *Acc. Chem. Res.* **2018**, *51*, 2641–2652.

(20) Larson, V. A.; Battistella, B.; Ray, K.; Lehnert, N.; Nam, W. Iron and manganese oxo complexes, oxo wall and beyond. *Nat. Rev. Chem* **2020**, *4*, 404–419.

(21) Kal, S.; Xu, S.; Que, L., Jr. Bio-inspired Nonheme Iron Oxidation Catalysis: Involvement of Oxoiron(V) Oxidants in Cleaving Strong C–H Bonds. *Angew. Chem., Int. Ed.* **2020**, *59*, 7332–7349.

(22) Dantignana, V.; Company, A.; Costas, M. Oxoiron(V) Complexes of Relevance in Oxidation Catalysis of Organic Substrates. *Isr. J. Chem.* **2020**, *60*, 1004–1018.

(23) Nam, W.; Lee, Y.-M.; Fukuzumi, S. Hydrogen Atom Transfer Reactions of Mononuclear Nonheme Metal–Oxygen Intermediates. *Acc. Chem. Res.* **2018**, *51*, 2014–2022.

(24) Lyakin, O. Y.; Bryliakov, K. P.; Talsi, E. P. Non-heme oxoiron(V) intermediates in chemo-, regio- and stereoselective oxidation of organic substrates. *Coord. Chem. Rev.* **2019**, *384*, 126–139.

(25) den Boer, D.; Hetterscheid, D. G. H. Design principles for homogeneous water oxidation catalysts based on first–row transition metals. *Curr. Opin. Electrochem.* **2022**, *35*, 101064.

(26) Collins, T. J. Designing Ligands for Oxidizing Complexes. *Acc. Chem. Res.* **1994**, *27*, 279–285.

(27) van Leest, N. P.; Tepaske, M. A.; Oudsen, J.-P. H.; Venderbosch, B.; Rietdijk, N. R.; Siegler, M. A.; Tromp, M.; van der Vlugt, J. I.; de Bruin, B. Ligand Redox Noninnocence in [Co^{III}(TAML)]$^{0/-}$ Complexes Affects Nitrene Formation. *J. Am. Chem. Soc.* **2020**, *142*, 552–563.

(28) Garrido-Barros, P.; Moonshiram, D.; Gil-Sepulcre, M.; Pelosin, P.; Gimbert-Suriñach, C.; Benet-Buchholz, J.; Llobet, A. Redox Metal–Ligand Cooperativity Enables Robust and Efficient Water Oxidation Catalysis at Neutral pH with Macrocyclic Copper Complexes. *J. Am. Chem. Soc.* **2020**, *142*, 17434–17446.

(29) Lim, J. H.; Engelmann, X.; Corby, S.; Ganguly, R.; Ray, K.; Soo, H. S. C–H activation and nucleophilic substitution in a photochemically generated high valent iron complex. *Chem. Sci.* **2018**, *9*, 3992–4002.

(30) Warner, G. R.; Mills, M. R.; Enslin, C.; Pattanayak, S.; Panda, C.; Panda, T. K.; Gupta, S. S.; Ryabov, A. D.; Collins, T. J. Reactivity and Operational Stability of N-Tailed TAMLs through Kinetic Studies of the Catalyzed Oxidation of Orange II by H$_2$O$_2$: Synthesis and X-ray Structure of an N-Phenyl TAML. *Chem.—Eur. J.* **2015**, *21*, 6226–6233.

(31) Collins, T. J.; Ryabov, A. D. Targeting of High-Valent Iron-TAML Activators at Hydrocarbons and Beyond. *Chem. Rev.* **2017**, *117*, 9140–9162.

(32) Lin, C.-W.; Chuang, Y.-W.; Lu, K.-Y.; Wang, Y.-H. First-Row Transition-Metal Complexes with Tetra-Amido Macrocyclic Ligands for Water and C(sp^3)–H Bond Oxidation: Performance Benchmarking Using Free Energy Relationships. *ChemCatChem* **2024**, *16*, No. e202301375.

(33) Xue, X.-S.; Ji, P.; Zhou, B.; Cheng, J.-P. The Essential Role of Bond Energetics in C–H Activation/Functionalization. *Chem. Rev.* **2017**, *117*, 8622–8648.

(34) Collins, T. J.; Powell, R. D.; Slebodnick, C.; Uffelman, E. S. Stable highly oxidizing cobalt complexes of macrocyclic ligands. *J. Am. Chem. Soc.* **1991**, *113*, 8419–8425.

(35) Ellis, W. C.; Tran, C. T.; Denardo, M. A.; Fischer, A.; Ryabov, A. D.; Collins, T. J. Design of More Powerful Iron-TAML Peroxidase Enzyme Mimics. *J. Am. Chem. Soc.* **2009**, *131*, 18052–18053.

(36) Palit, D.; Kundu, S.; Pain, P. K.; Sarma, R.; Manna, D. A Chemical Model of a TET Enzyme for Selective Oxidation of Hydroxymethyl Cytosine to Formyl Cytosine. *Inorg. Chem.* **2023**, *62*, 10039–10043.

(37) Ghosh, A.; Tiago de Oliveira, F.; Yano, T.; Nishioka, T.; Beach, E. S.; Kinoshita, I.; Münck, E.; Ryabov, A. D.; Horwitz, C. P.; Collins, T. J. Catalytically Active μ-Oxodiiron(IV) Oxidants from Iron(III) and Dioxygen. *J. Am. Chem. Soc.* **2005**, *127*, 2505–2513.

(38) Das, A.; Nutting, J. E.; Stahl, S. S. Electrochemical C–H oxygenation and alcohol dehydrogenation involving Fe-oxo species using water as the oxygen source. *Chem. Sci.* **2019**, *10*, 7542–7548.

(39) Chandra, B.; Hellan, K. M.; Pattanayak, S.; Gupta, S. S. Oxoiron(v) mediated selective electrochemical oxygenation of unactivated C–H and C = C bonds using water as the oxygen source. *Chem. Sci.* **2020**, *11*, 11877–11885.

(40) Du, H.-Y.; Chen, S.-C.; Su, X.-J.; Jiao, L.; Zhang, M.-T. Redox-Active Ligand Assisted Multielectron Catalysis: A Case of Co^{III} Complex as Water Oxidation Catalyst. *J. Am. Chem. Soc.* **2018**, *140*, 1557–1565.

(41) Zhang, X.-M.; Bordwell, F. G. Homolytic bond dissociation energies of the benzylic carbon-hydrogen bonds in radical anions and radical cations derived from fluorenes, triphenylmethanes, and related compounds. *J. Am. Chem. Soc.* **1992**, *114*, 9787–9792.

(42) Rafiee, M.; Abrams, D. J.; Cardinale, L.; Goss, Z.; Romero-Arenas, A.; Stahl, S. S. Cyclic voltammetry and chronoamperometry: mechanistic tools for organic electrosynthesis. *Chem. Soc. Rev.* **2024**, *53*, 566–585.

(43) Sandford, C.; Edwards, M. A.; Klunder, K. J.; Hickey, D. P.; Li, M.; Barman, K.; Sigman, M. S.; White, H. S.; Minteer, S. D. A synthetic chemist's guide to electroanalytical tools for studying reaction mechanisms. *Chem. Sci.* **2019**, *10*, 6404–6422.

(44) Chakrabarti, S.; Sinha, S.; Tran, G. N.; Na, H.; Mirica, L. M. Characterization of paramagnetic states in an organometallic nickel hydrogen evolution electrocatalyst. *Nat. Commun.* **2023**, *14*, 905.

(45) Sastri, C. V.; Lee, J.; Oh, K.; Lee, Y. J.; Lee, J.; Jackson, T. A.; Ray, K.; Hirao, H.; Shin, W.; Halfen, J. A.; et al. Axial ligand tuning of a nonheme iron(IV)–oxo unit for hydrogen atom abstraction. *Proc. Natl. Acad. Sci. U.S.A.* **2007**, *104*, 19181–19186.

(46) Warm, K.; Paskin, A.; Kuhlmann, U.; Bill, E.; Swart, M.; Haumann, M.; Dau, H.; Hildebrandt, P.; Ray, K. A Pseudotetrahedral Terminal Oxoiron(IV) Complex: Mechanistic Promiscuity in C–H Bond Oxidation Reactions. *Angew. Chem., Int. Ed.* **2021**, *60*, 6752–6756.

(47) Casadevall, C.; Bucci, A.; Costas, M.; Lloret-Fillol, J. Chapter Four - Water oxidation catalysis with well-defined molecular iron

complexes. In *Adv. Inorg. Chem.*; van Eldik, R., Hubbard, C. D., Eds.; Academic Press, 2019; Vol. 74; pp 151−196.

(48) Hsu, W.-C.; Wang, Y.-H. Homogeneous Water Oxidation Catalyzed by First-Row Transition Metal Complexes: Unveiling the Relationship between Turnover Frequency and Reaction Overpotential. *ChemSusChem* **2022**, *15*, No. e202102378.

(49) Chandra, B.; De, P.; Sen Gupta, S. Selective oxygenation of unactivated C−H bonds by dioxygen via the autocatalytic formation of oxoiron(v) species. *Chem. Commun.* **2020**, *56*, 8484−8487.

(50) Ghosh, M.; Pattanayak, S.; Dhar, B. B.; Singh, K. K.; Panda, C.; Sen Gupta, S. Selective C−H Bond Oxidation Catalyzed by the Fe-bTAML Complex: Mechanistic Implications. *Inorg. Chem.* **2017**, *56*, 10852−10860.

(51) Pattanayak, S.; Jasniewski, A. J.; Rana, A.; Draksharapu, A.; Singh, K. K.; Weitz, A.; Hendrich, M.; Que, L., Jr.; Dey, A.; Sen Gupta, S. Spectroscopic and Reactivity Comparisons of a Pair of bTAML Complexes with Fe^V=O and Fe^{IV}=O Units. *Inorg. Chem.* **2017**, *56*, 6352−6361.

(52) Ghosh, M.; Singh, K. K.; Panda, C.; Weitz, A.; Hendrich, M. P.; Collins, T. J.; Dhar, B. B.; Sen Gupta, S. Formation of a Room Temperature Stable $Fe^V(O)$ Complex: Reactivity Toward Unactivated C−H Bonds. *J. Am. Chem. Soc.* **2014**, *136*, 9524−9527.

(53) Jana, S.; Pattanayak, S.; Das, S.; Ghosh, M.; Velasco, L.; Moonshiram, D.; Sen Gupta, S. Comparing the reactivity of an oxoiron(iv) cation radical and its oxoiron(v) tautomer towards C−H bonds. *Chem. Commun.* **2023**, *59*, 2755−2758.

(54) Lu, X.; Lee, Y.-M.; Sankaralingam, M.; Fukuzumi, S.; Nam, W. Catalytic Four-Electron Reduction of Dioxygen by Ferrocene Derivatives with a Nonheme Iron(III) TAML Complex. *Inorg. Chem.* **2020**, *59*, 18010−18017.

(55) Chandra, B.; Singh, K. K.; Gupta, S. S. Selective photocatalytic hydroxylation and epoxidation reactions by an iron complex using water as the oxygen source. *Chem. Sci.* **2017**, *8*, 7545−7551.

(56) Bell, R. P.; Hinshelwood, C. N. The theory of reactions involving proton transfers. *Proc. R Soc. Lond. A* **1997**, *154*, 414−429.

(57) Evans, M. G.; Polanyi, M. Inertia and driving force of chemical reactions. *Trans. Faraday Soc.* **1938**, *34*, 11−24.

(58) Evans, M. G.; Polanyi, M. Further considerations on the thermodynamics of chemical equilibria and reaction rates. *Trans. Faraday Soc.* **1936**, *32*, 1333−1360.

(59) Wang, Y.-H.; Mondal, B.; Stahl, S. S. Molecular Cobalt Catalysts for O_2 Reduction to H_2O_2: Benchmarking Catalyst Performance via Rate−Overpotential Correlations. *ACS Catal.* **2020**, *10*, 12031−12039.

(60) Wang, Y.-H.; Pegis, M. L.; Mayer, J. M.; Stahl, S. S. Molecular Cobalt Catalysts for O_2 Reduction: Low-Overpotential Production of H_2O_2 and Comparison with Iron-Based Catalysts. *J. Am. Chem. Soc.* **2017**, *139*, 16458−16461.

(61) Rountree, E. S.; McCarthy, B. D.; Eisenhart, T. T.; Dempsey, J. L. Evaluation of Homogeneous Electrocatalysts by Cyclic Voltammetry. *Inorg. Chem.* **2014**, *53*, 9983−10002.

(62) Luo, Y.-R. *Comprehensive Handbook of Chemical Bond Energies*; CRC Press, 2007.

(63) Lu, X.; Li, X.-X.; Lee, Y.-M.; Jang, Y.; Seo, M. S.; Hong, S.; Cho, K.-B.; Fukuzumi, S.; Nam, W. Electron-Transfer and Redox Reactivity of High-Valent Iron Imido and Oxo Complexes with the Formal Oxidation States of Five and Six. *J. Am. Chem. Soc.* **2020**, *142*, 3891−3904.

(64) Jana, S.; De, P.; Dey, C.; Dey, S. G.; Dey, A.; Gupta, S. S. Highly regioselective oxidation of C−H bonds in water using hydrogen peroxide by a cytochrome P450 mimicking iron complex. *Chem. Sci.* **2023**, *14*, 10515−10523.

(65) Nakada, A.; Matsumoto, T.; Chang, H.-C. Redox-active ligands for chemical, electrochemical, and photochemical molecular conversions. *Coord. Chem. Rev.* **2022**, *473*, 214804.